Short-T_R, Coherent, Gradient Echo Imaging

OVERVIEW

The focus of this unit is on understanding the build-up of the magnetization to steady-state and the practical implementation of the simplest forms of imaging in the steady-state. When a spin system is repeatedly disturbed by a fast repetition of RF pulses, the transverse magnetization after each new RF pulse approaches a steady-state value which is smaller than the thermal equilibrium value. The spin system takes a finite number of pulses before this steady-state is reached in a time that depends on both the T_1 of the tissue and the flip angle of the RF pulse.

Sequences utilizing a steady-state approach can be broadly classified as steady-state coherent (SSC) and steady-state incoherent (SSI) sequences. The main difference between the two lies in whether or not the transverse magnetization is zero between successive RF pulses. For SSC sequences, both transverse and longitudinal magnetization components at the end of a repetition period contribute to the signal in the next cycle, leading to a different overall magnetization response. The SSC behavior is the subject of this unit.

Figures B5.2.1 and B5.2.2 are two examples of how the steady state can be reached when all magnetization components are accounted for from one RF cycle to the next one. To reach a steady state, the phase of spins must be kept constant from one RF pulse to the next. This requires balancing the gradients along each direction. Such a fully balanced sequence is shown in Figure B5.2.3. This type of sequence is usually referred to as an SSFP (steady state free precession) sequence. Balancing the sequence only guarantees that the phase of the transverse magnetization is the same from pulse to pulse. This phase, also known as the resonance offset, is generated by the RF pulse phase and local field inhomogeneities. As this phase changes, so will the steady state magnetization, and, hence, the contrast in the MR images.

Figure B5.2.4 shows the transverse magnetization at two different flip angles against the resonance offset angle. One can see that a higher signal can be obtained if a large flip angle and a 180° resonance offset angle are used. This signal can be as high as 0.35 of the maximum value. A comparison of phantom images between two different flip angles and two resonance offset angles is shown in Figure B5.2.5. A comparison of human images between two different resonance offset angles is shown in Figure B5.2.7. When the resonance offset angle is about π, the SSC image can be considered as a T_2/T_1-weighted image (Fig. B5.2.7B). This can be compared to the conventional T_1-weighted image (Fig. B5.2.7C) and T_2-weighted image (Fig. B5.2.7D).

Current emphasis for SSFP images is for MR angiography with some potential for myelographic applications. This method is currently under active research investigation. It is very sensitive to local field inhomogeneities, but, with current high gradient capabilities, very short T_R sequences suffer less and less from this problem.

TECHNICAL DISCUSSION

This section presents detailed derivations of expressions for the steady-state magnetization and its approach to steady-state coherent equilibrium.

Contributed by Yu-Chung Norman Cheng and E. Mark Haacke

Current Protocols in Magnetic Resonance Imaging (2001) B5.2.1-B5.2.12

General Concept

When T_R is on the order of, or less than, T_2, and no attempt is made to spoil the transverse magnetization, there will be a coherent build-up of signal towards a steady-state value which is a mixture of longitudinal and transverse components present at the initial state. This dependence on the initial magnetization is illustrated in Figures B5.2.1 and B5.2.2 by assuming two different initial conditions. In Figure B5.2.1, it is assumed that equal magnetization exists along both y and z axes, while in Figure B5.2.2 it is assumed that equal magnetization components exist along all three axes.

From Figures B5.2.1 and B5.2.2, it is also seen that the steady-state magnetization components depend on the field seen by the isochromat of interest. That is, two isochromats seeing different static fields will reach different steady-state values after free precession. The steady-state magnetization also depends on the flip angle, the initial magnetization components, and T_R. Further, in Figures B5.2.1 and B5.2.2, the events that were followed carefully were the initial condition existing just before an RF pulse, the immediate effect of the RF pulse, and the final condition created at the end of the free precession period, without paying much attention to the details of how the final condition was achieved. The steady-state magnetization is determined by the total precession angle of the transverse magnetization components during each T_R, depending on the quantity:

$$\beta_{\text{total}}(T_R) = \gamma \Delta B T_R + \gamma \vec{r} \cdot \int_0^{T_R} \vec{G}(t)dt \qquad \textbf{(B5.2.1)}$$

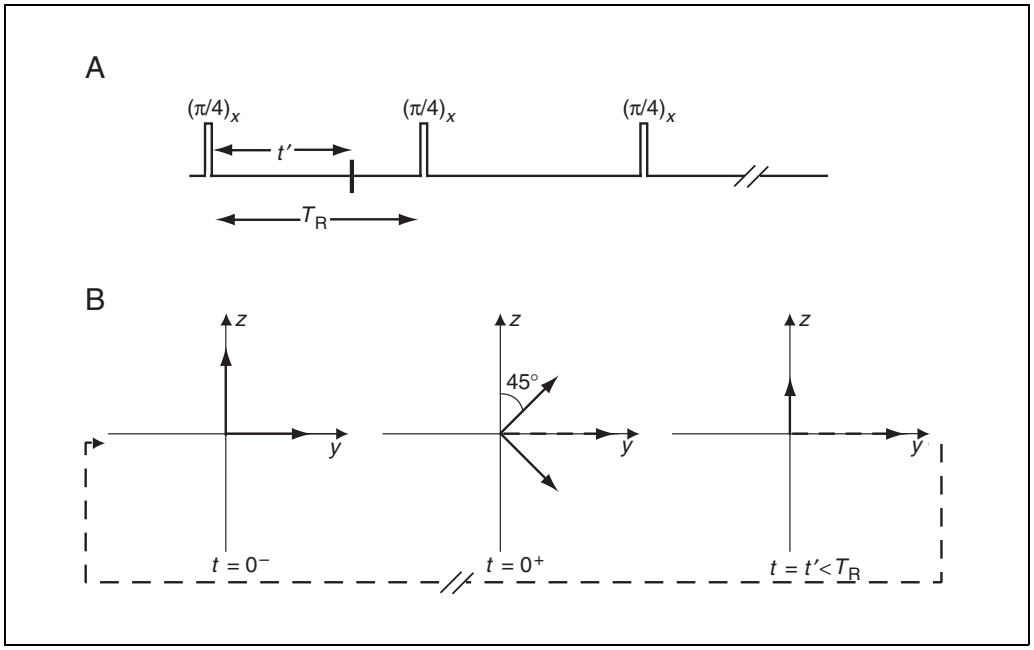

Figure B5.2.1 Demonstration of coherent steady-state formation. (**A**) Sequence diagram showing an RF pulse repetition example which leads to a steady-state. (**B**) The case when equal magnetization is available along the y and z axes at the beginning of a free precession period, and a 45°-pulse is applied along the x axis. The effective z magnetization after the RF pulse is zero. Assume that the magnetization considered here is from a resonant isochromat of spins. Their precession angle in the rotating frame is zero, leaving them all along $\hat{y}$ throughout the evolution period. It is now easy to visualize that, depending on the T_R value, the y magnetization decays due to T_2 decay while the z magnetization recovers towards M_0 and, at the end of the evolution period, the magnetization state returns to the value it had just before the previous RF pulse, leading to a steady-state.

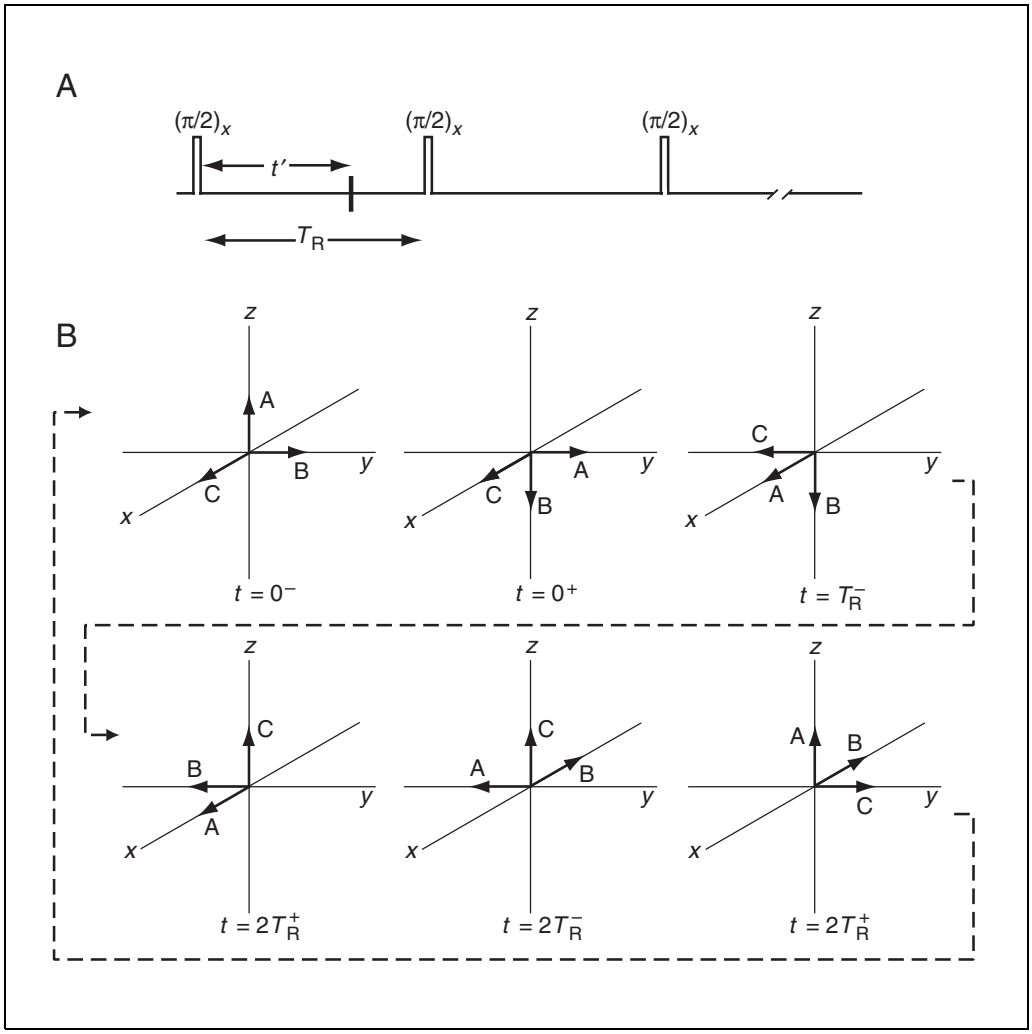

Figure B5.2.2 (**A**) Sequence diagram showing a second RF pulse repetition example which leads to a different steady-state. (**B**) Steady-state formation with equal *x*, *y* and *z* components just before the first RF pulse. After the first π/2-pulse applied along the *x*-direction, the presence of a B_0 inhomogeneity is assumed to cause a π/2 precession of transverse magnetization during the evolution period. Following the second RF pulse, the third free precession period leads to the initial condition (at $t = 0^-$), thereby creating the required periodicity to reach steady state. This is indicated by the arrow going from the state at $t = 2T_R^+$ to the state at $t = 0^-$. It is also assumed that T_R is so short that all relaxation effects can be neglected.

where the two terms are the static and gradient field inhomogeneity–induced resonance offset angles, respectively. The quantity β_{total} is referred to as the resonance offset angle.

In order to reach steady state, all the imaging gradients used must have zero zeroth moment over each repetition period, i.e., they should all be "balanced" over each repetition period. Such a balanced gradient coherent steady-state sequence implementation is shown in Figure B5.2.3. The resonance offset is then determined by the free precession caused by the background field inhomogeneities and not the imaging gradients. Hence, it is called steady state free precession (SSFP). It is common to use the term "SSFP sequence" in the MR imaging literature to loosely mean a balanced gradient coherent steady-state sequence. The terms SSC sequence and SSFP sequence are interchangeably used in this sense in the text too. For the rest of the discussion in this unit, it is assumed that all imaging gradients used in the sequence are balanced; thereby the resonance offset angle depends only on the static field inhomogeneities. For this reason, the subscript total is dropped from β_{total} for the remaining part of this unit.

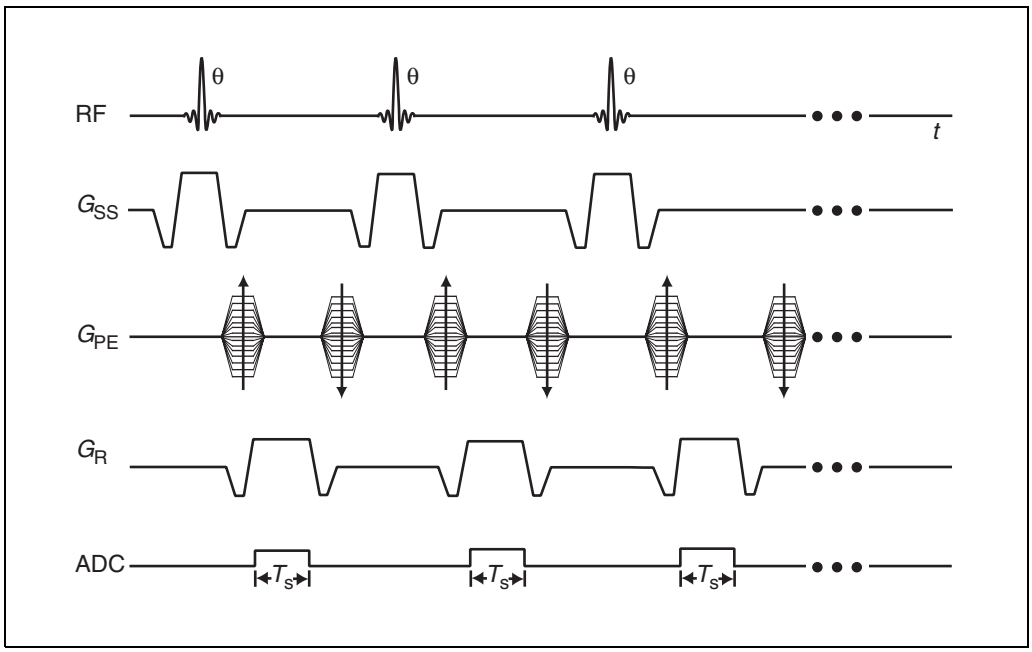

Figure B5.2.3 A typical SSC imaging sequence implementation. Note the balancing of all imaging gradients to let all isochromats evolve under equivalent free precession conditions over each repetition period unaffected by a particular phase encoding or read gradient structure.

Steady-State Free Precession: The Equilibrium Signal

We will find the equilibrium solution under a variety of conditions which affect the phase of the transverse magnetization. Let $\beta(t) = \Delta\omega \cdot t$ with $\Delta\omega = \omega_0 - \omega = \gamma\Delta B$. Here, $\Delta\omega$ is referred to as the *resonance offset frequency*, and $\beta(T_R)$, the *resonance offset (angle)*. For $nT_R \le t \le (n+1)T_R$, $t' = t - nT_R$, and the argument n representing the time nT_R, a solution of the Bloch equation after the (n + 1)st RF pulse is:

$$M_x(n,t') = [M_x^+(n)\cos\beta(t') + M_y^+(n)\sin\beta(t')]e^{-t'/T_2} \quad \textbf{(B5.2.2)}$$

$$M_y(n,t') = [-M_x^+(n)\sin\beta(t') + M_y^+(n)\cos\beta(t')]e^{-t'/T_2} \quad \textbf{(B5.2.3)}$$

$$M_z(n,t') = M_z^+(n)e^{-t'/T_1} + M_0(1-e^{-t'/T_1}) \quad \textbf{(B5.2.4)}$$

(The precession is in the transverse plane because we assume that ΔB is along the z-direction.) For a clockwise rotation about $\hat{x}$, the matrix representation for Equation B5.2.2 to Equation B5.2.4 is found using:

$$R_x(\theta) = \begin{pmatrix} 1 & 0 & 0 \\ 0 & \cos\theta & \sin\theta \\ 0 & -\sin\theta & \cos\theta \end{pmatrix} \quad \textbf{(B5.2.5)}$$

with:

$$D(t') = \begin{pmatrix} e^{-t'/T_2}\cos\beta(t') & e^{-t'/T_2}\sin\beta(t') & 0 \\ -e^{-t'/T_2}\sin\beta(t') & e^{-t'/T_2}\cos\beta(t') & 0 \\ 0 & 0 & e^{-t'/T_1} \end{pmatrix} \quad \textbf{(B5.2.6)}$$

With these definitions:

$$\vec{M}^{+}(n) = R_x(\theta)\vec{M}^{-}(n) \quad \textbf{(B5.2.7)}$$

and:

$$\vec{M}^{-}(n+1) = D(T_R)\vec{M}^{+}(n) + M_0(1-E_1)\hat{z} \quad \textbf{(B5.2.8)}$$

where $E_1 \equiv e^{-T_R/T_1}$. Now, $\vec{M}^{-}(n+1)$ can be set equal to $\vec{M}^{-}(n)$ to find the steady-state value.

The solutions are quite simple and compact in matrix form. From Equation B5.2.7 and Equation B5.2.8, as n approaches ∞,

$$\vec{M}^{-}(\infty) = (I - D(T_R)R_x(\theta))^{-1} M_0(1-E_1)\hat{z} \quad \textbf{(B5.2.9)}$$

The final solutions are:

$$M_x^{-}(\infty) = M_0(1-E_1)\frac{E_2\sin\theta\sin\beta}{d} \quad \textbf{(B5.2.10)}$$

$$M_y^{-}(\infty) = M_0(1-E_1)\frac{E_2\sin\theta(\cos\beta - E_2)}{d} \quad \textbf{(B5.2.11)}$$

$$M_z^{-}(\infty) = M_0(1-E_1)\frac{[(1-E_2\cos\beta) - E_2\cos\theta(\cos\beta - E_2)]}{d} \quad \textbf{(B5.2.12)}$$

and:

$$M_x^{+}(\infty) = M_x^{-}(\infty) \quad \textbf{(B5.2.13)}$$

$$M_y^{+}(\infty) = M_0(1-E_1)\frac{\sin\theta(1-E_2\cos\beta)}{d} \quad \textbf{(B5.2.14)}$$

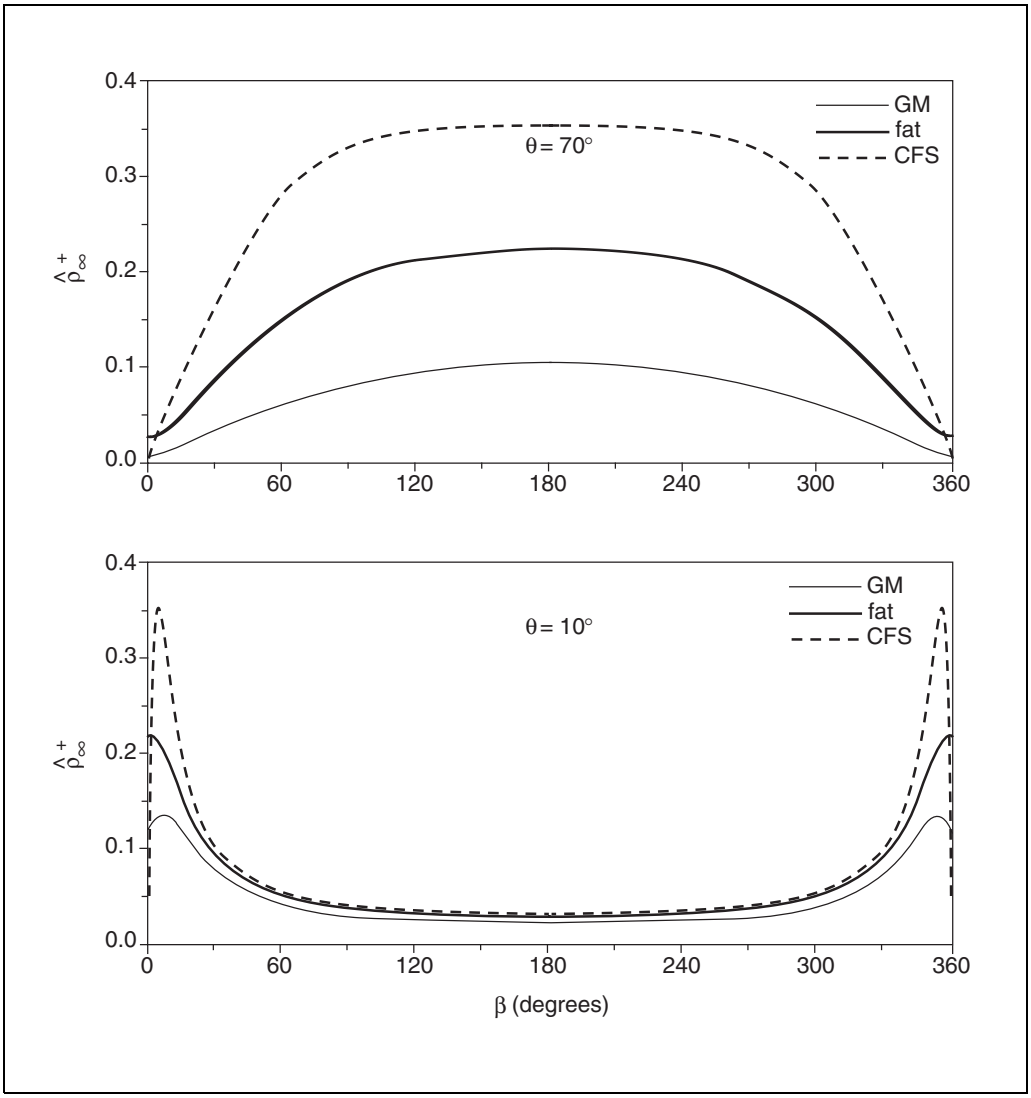

Figure B5.2.4 Plot of the magnitude of the steady-state voxel signal, $\hat{\rho}_{\infty+} \equiv M_{\perp}^{+}(\infty)$, as a function of β for different tissues for θ = 70° and θ = 10°. A T_R of 10 msec and a T_E of 0 msec were assumed. GM represents gray matter and CSF, cerebrospinal fluid.

$$M_z^+(\infty) = M_0(1-E_1)\frac{[E_2(E_2-\cos\beta)+(1-E_2\cos\beta)\cos\theta]}{d} \qquad \textbf{(B5.2.15)}$$

where $E_2 \equiv e^{-T_R/T_2}$ and:

$$d = (1-E_1\cos\theta)(1-E_2\cos\beta) - E_2(E_1-\cos\theta)(E_2-\cos\beta) \qquad \textbf{(B5.2.16)}$$

In full form, the SSFP signal is a complicated function of θ, E_1, E_2 and β. The dependence on θ and β is summarized for different tissues in Figure B5.2.4 for a choice of $T_R << T_2$ for all the tissues. These plots show that for small flip angles (for example, see the curves for θ = 10°), a large signal response is achieved only when β is close to 0° or 360°. On the other hand, for large flip angles (for example, see curves for θ = 70°), a uniformly high signal is obtained for a range of β values centered around β = 180°.

Short-T_R, Coherent, Gradient Echo Imaging

Since the static field varies as a function of position, β varies as a function of position within the image and, typically, this leads to signal variation for SSC images of homoge-

neous objects. However, $\Delta B(\vec{r})$ does not usually vary over a single voxel. As a result, each voxel can be considered an isochromat whose signal expression is defined based on Equation B5.2.10 to Equation B5.2.15. Practically, if there is a significant field variation across the object, this will lead to a changing $\beta(\vec{r})$ and the dependence of the magnetization components on the resonance offset angle (see Fig. B5.2.4) means that uniformity will be degraded in the reconstructed image. The measured signal in a voxel for a given echo time will be found by integrating $M_{\perp}^{+}(\infty)\, e^{-T_E/T_2}$ over the physical distribution of β values present in that voxel. Up to this point, all field dependence is carried by β and, therefore, E_2 should not be replaced by E_2^* even though this is a gradient echo experiment. *The above*

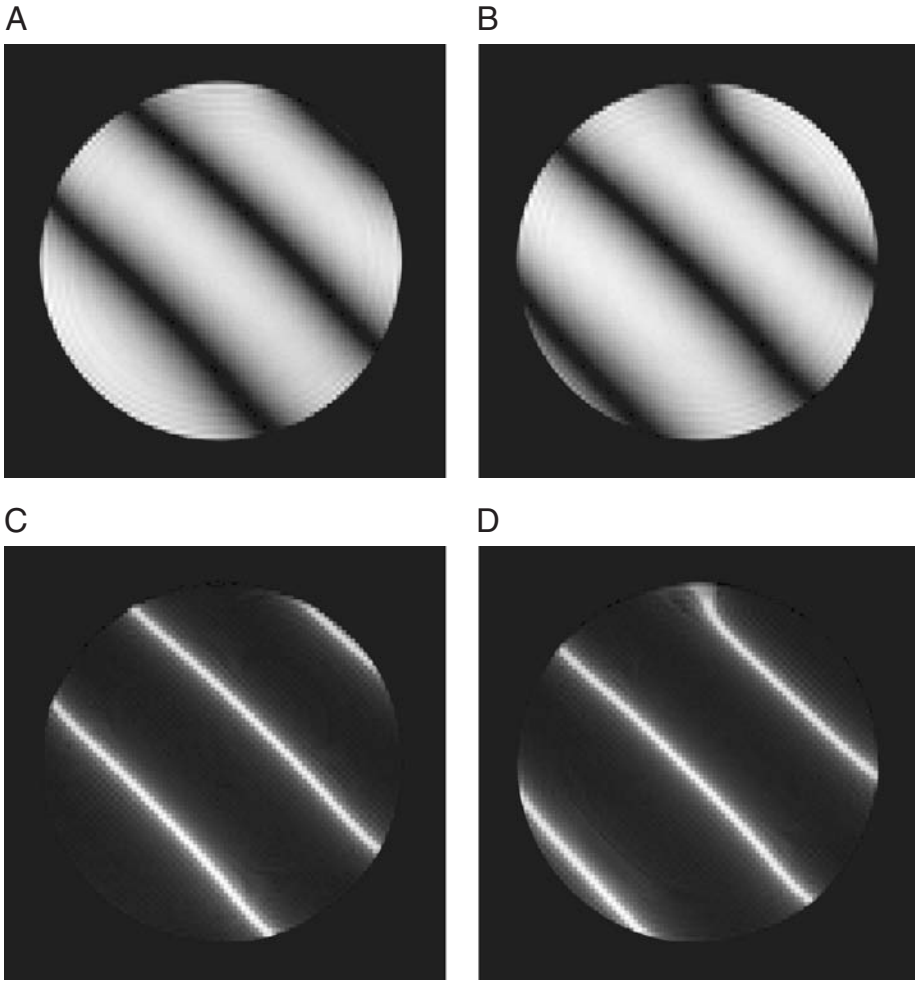

Figure B5.2.5 Images of a homogeneous phantom obtained using an SSFP sequence. A T_R of 7 msec was used to image the phantom which had a T_1 of 350 msec and T_2 of 200 msec. Images (**A**) and (**B**) were obtained using non-alternating (i.e., $\beta_{RF} = 0$) and alternating (i.e., $\beta_{RF} = \pi$) RF pulses, respectively, at a flip angle of 90°. Images (**C**) and (**D**) were obtained with a flip angle of 2° also with nonalternating and alternating RF pulses, respectively. The background field homogeneity was changed by adding a gradient offset of 0.004 mT/m along both the read and phase encoding directions, resulting in a linearly varying resonance offset along a 45° angle as displayed by the valleys and peaks in the signal in these images. Imaging parameters: (A), (B) T_R/T_E = 7 msec/3.3 msec, T_s = 2.56 msec, $\Delta x \times \Delta y \times \Delta z$ = 1.0 mm × 1.0 mm × 1.0 mm, $N_x \times N_y \times N_z = 256 \times 256 \times 32$, $\theta = 90°$, $N_{acq} = 1$, τ_{RF} = 0.512 msec, G_{ss} = 5.73 mT/m; (C), (D) $\theta = 2°$.

mentioned integration is what may eventually lead to e^{-T_E/T_2} being replaced by e^{-T_E/T_2^*} in the voxel.

However, if β remains close to 180°, this is not problematic as long as the variation in β across the object is small. This is typically achieved by shimming the field well, and keeping T_R as short as possible. On the other hand, if $\beta(\vec{r})$ ranges in the neighborhood of 0° or 360°, the signal variation is drastically enhanced.

The question arises at this point as to how $\beta(\vec{r})$ can be biased around π to obtain a homogeneous image. An additional means to change the resonance offset angle other than using an unbalanced gradient is to make the RF phase a function of RF pulse number, typically by incrementing the phase linearly. The linear RF phase increment is represented by the quantity β_{RF}. Although the steady-state magnetization in the presence of a linear RF phase increment does not conform to the solutions of Equation B5.2.10 to Equation B5.2.15, in the general case, it can be shown that the steady-state magnetization satisfies these equations when β_{RF} equals 180°, with β effectively replaced by $(\beta + \pi)$. Now, signal uniformity can be preserved for large flip angles by keeping $\gamma \Delta B T_R$ small. These effects and the contrasting signal behavior as functions of β for small flip angle versus large flip angle excitation are summarized in the imaging results obtained on a homogeneous phantom shown in Figure B5.2.5. As seen from Figure B5.2.4, these images show peak signal on the low flip angle images (Fig. B5.2.5C and Fig. B5.2.5D) only where the signal in the corresponding RF alternated large flip angle image (Fig. B5.2.5A and Fig. B5.2.5B, respectively) is at its lowest. Similarly, note the transformation of low signal areas into peak signal areas between the non-alternated (i.e., $\beta_{RF} = 0$, Fig. B5.2.5A and Fig. B5.2.5C) and alternated RF (i.e., $\beta_{RF} = \pi$, Fig. B5.2.5B and Fig. B5.2.5D, respectively) image acquisitions. It is seen that if the local ΔB value causes the signal to be low in one image, the same inhomogeneity causes the signal to be high in the other image (see the structure indicated by the filled arrow and the blood vessel indicated by the open arrow in Fig. B5.2.7, for example). Evidently, a homogeneous image can be obtained by choosing the higher of the two voxel signal values on a pixel-by-pixel basis throughout the image.

Approach to Coherent Steady-State

As in the case of incoherent steady-state, the magnetization takes a finite time to reach steady-state in the coherent or unspoiled case as well. For two arbitrary initial magnetization vector conditions, this was qualitatively shown to vary depending on the resonance offset angle and flip angle in Figures B5.2.1 and B5.2.2. A further look at the steady-state magnetization components defined in Equation B5.2.10 to Equation B5.2.15 tells us that the approach to steady-state also depends on T_1, T_2 and T_R. The complicated dependence of the SSC signal on these quantities makes an analytical writing of the approach to steady-state along lines similar to the SSI case very complicated. For this reason, an understanding of the dependence on these parameters can be obtained only by Bloch equation simulation for a fixed set of values of β, T_R and θ for a given tissue of interest. A plot showing the multiparameter dependence of the approach to steady-state for different tissues (i.e., different E_1 and E_2 values) is given in Figure B5.2.6. The approach to steady-state is also changed by changing the flip angle or β. As in the SSI case, the different magnetization components reach steady-state in a time which is on the order of T_1 (see *UNIT B5.1*).

Utility of SSC Imaging

Steady-state coherent imaging is of practical interest despite its complicated signal behavior. To appreciate this, it is instructive to examine the limit $T_R << T_2$, T_1 with β set to either zero or π. In either case, $M_x^+ = 0$. When $\beta = \pi$:

$$M_y^+(\infty) = \frac{M_0(1-E_1)\sin\theta}{(1-E_1\cos\theta)-E_2(E_1-\cos\theta)}$$
$$\simeq \frac{M_0\sin\theta}{\left(\frac{T_1}{T_2}+1\right)-\cos\theta\left(\frac{T_1}{T_2}-1\right)} \qquad \textbf{(B5.2.17)}$$

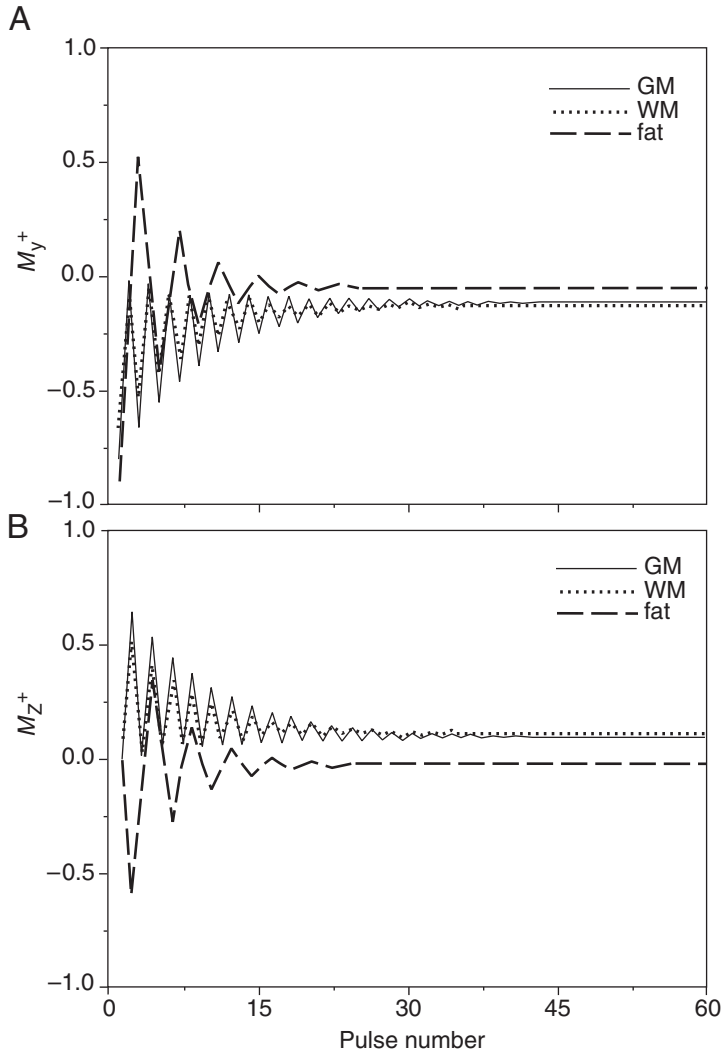

Figure B5.2.6 Approach to steady-state of M_y^+ and M_z^+ for three different tissues at a T_R of 20 msec for $\theta = \pi/2$ and $\beta = 180°$. (**A**) M_y^+ as a function of RF pulse number *n*. (**B**) M_z^+ as a function of RF pulse number *n*. M_x^+ is not shown for this case since the above plots were generated by assuming thermal equilibrium initial conditions and, for this particular initial condition, M_x^+ is zero throughout the experiment. The additional chemical shift-induced resonance offset angle for fat is assumed to be 8π, so that the effective (total) resonance offset angle for fat in the plot is 9π. GM represents gray matter and WM, white matter.

as both E_1 and E_2 can be approximated with $[1 - (T_R/T_1)]$ and $[1 - (T_R/T_2)]$, respectively. Therefore, the contrast obtained with an SSFP sequence is essentially T_2/T_1-weighted, which is yet another form of contrast available in MRI.

The optimal signal as a function of flip angle for a fixed β can be shown to occur at the flip angle θ_{opt} such that:

$$\cos\theta_{opt} = \frac{E_1 + E_2(\cos\beta - E_2)/(1 - E_2\cos\beta)}{1 + E_1E_2(\cos\beta - E_2)/(1 - E_2\cos\beta)} \quad \textbf{(B5.2.18)}$$

In the case when $\beta \simeq \pi$, i.e., the alternating RF case for the short T_R limit, the above expression approximates to:

$$\cos\theta_{opt} \simeq \frac{T_1/T_2 - 1}{T_1/T_2 + 1} \quad \textbf{(B5.2.19)}$$

with the peak signal being proportional to:

$$M_y^+(\infty)\Big|_{\theta=\theta_{opt}} \simeq \frac{1}{2}M_0\sqrt{\frac{T_2}{T_1}} \quad \textbf{(B5.2.20)}$$

It is seen from Equation B5.2.20 that tissues whose T_2-to-T_1 ratios are high have high signal. For example, for a tissue such as CSF (cerebrospinal fluid), whose T_1-to-T_2 ratio is ~2 (see Table B5.1.1), θ_{opt} equals 70°. At this flip angle, the peak signal for $\beta = \pi$ is found from Equation B5.2.20 to be ~$0.35M_0$ (see also Fig. B5.2.4). That is, at short T_R, a signal which equals 35% of the highest signal that can ever be attained for CSF is obtained (in the infinite T_R limit, the signal is given by M_0). Another interesting phenomenon which is noted in Figure B5.2.4 is that CSF has the same peak signal response (~0.35 M_0) even in the low flip angle regime. This leads to a very interesting high signal regime: if the background static field can be designed such that all isochromats experience a ΔB which leads the unique value of β where this peak value occurs, a large signal is obtained at short T_R values with small flip angle excitation. This may prove very useful for enhancing CSF signal at high fields while keeping RF power desposition to a minimum.

One can see that SSC images are T_2/T_1-weighted from Equation B5.2.20. This is demonstrated in images of the brain shown in Figure B5.2.7. Since CSF has the highest T_2-to-T_1 ratio (see Table B5.1.1), it has the highest signal. On the other hand, gray matter (GM) and white matter (WM) appear about the same because of their comparable T_2-to-T_1 ratios. This effect is further demonstrated by comparing this different contrast mechanism with the more common T_1 and T_2-weighted contrast (see Figs. B5.2.7C and B5.2.7D). Another important point is the complementarity of images acquired with non-alternating RF and alternating RF (Figs. B5.2.7A and B5.2.7B). That is, as in Figure B5.2.5, dark and bright regions reverse when the RF switches from alternating to non-alternating.

Equation B5.2.20 shows that SSC imaging represents the most efficient way to collect data for a given tissue using as short a T_R as possible. This T_R independence of the SSC signal leads to a T_R independent SNR as long as T_R can be reduced without a concomitant decrease in T_s and hence increase the noise. In comparison, the signal at the optimal flip angle for SSI imaging (i.e., $\theta = \theta_E$) is proportional to $\sqrt{T_R}$ for short T_R (see *UNIT B5.1*). The T_R independence of the SSC signal has been untapped until now for several reasons. One relates to available gradient strengths and the other to the background field inhomogeneity. For example, if T_R = 10 msec (which is easily achievable on commercial scanners for 1

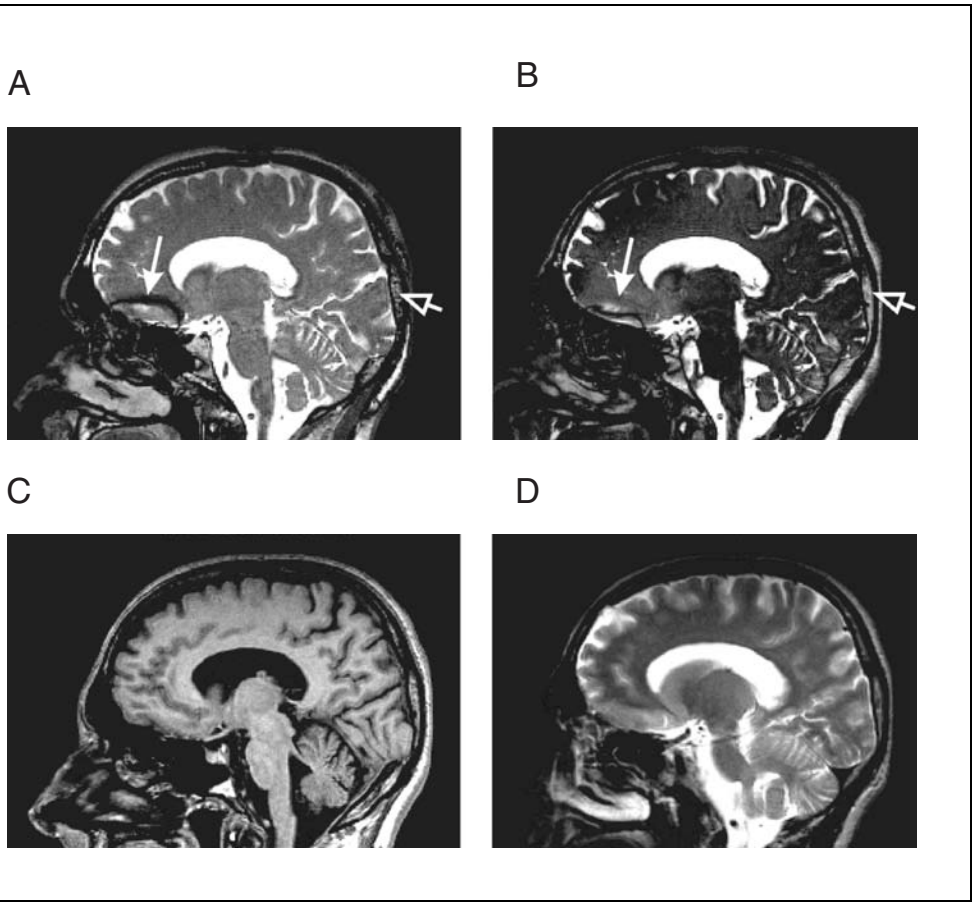

Figure B5.2.7 Images obtained with a fully-balanced 3-D SSC imaging sequence: (**A**) non-alternating RF (i.e., $\beta_{RF} = 0$) (**B**) alternating RF (i.e., $\beta_{RF} = \pi$). (**C**) A T_1-weighted image and (**D**) a T_2-weighted image at the same slice location are shown for comparison. The T_2-weighted image in (D) is a thicker slice (5 mm thick in comparison with 2 mm thick slices for the others). Hence, the slight difference in anatomical depiction from the other three images. Imaging parameters: (A), (B) T_R/T_E = 7 msec/3.3 msec, T_s = 2.56 msec, $\Delta x \times \Delta y \times \Delta z$ = 1.0 mm × 1.0 mm × 2.0 mm, $N_x \times N_y \times N_z = 256 \times 256 \times 96$, $\theta = 35°$, $N_{acq} = 1$, τ_{RF} = 0.512 msec, G_{ss} = 0.96 mT/m; (C) T_R/T_E = 30 msec/5.4 msec, T_s = 5.12 msec, $\theta = 25°$, τ_{RF} = 1.28 msec, G_{ss} = 1.15 mT/m; (D) T_R/T_E = 7000 msec/90 msec, T_s = 7.68 msec, $\Delta x \times \Delta y \times \Delta z$ = 1.0 mm × 1.0 mm × 5.0 mm, $N_x \times N_y = 256 \times 256$, $\theta = 90°$, τ_{RF} = 2.56 msec, G_{ss} = 2.4 mT/m.

mm^3 voxels in 3-D imaging), only a ΔB of ~0.75 ppm is required to create a resonance offset range of π at 1.5 T. Practically, this type of inhomogeneity can easily occur across the brain depending on the success of the shim procedure. As discussed earlier, this leads to image signal inhomogeneity and also a T_R dependence of the signal. The shorter T_R can be made, the less of a problem ΔB will be. Overall, as magnet homogeneity improves, with better shimming and faster gradient switching capability, there will be an increasing number of applications of extremely short-T_R SSC imaging.

KEY REFERENCES

Bydder, G.M. and Young, I.R. 1985. Clinical use of the partial and saturation recovery sequences in MR imaging. *J. Comput. Assist. Tomogr.* 9:1020.

This paper proposed different short T_E, fast imaging methods.

Ernst, R.R. and Anderson, W.A. 1966. Application of Fourier transform spectroscopy to magnetic resonance. *Rev. Sci. Instrum.* 37:93.

This article covers both the coherent and incoherent steady-states and gives expressions for flip angles which maximize the signal (hence the name "Ernst angle").

Haacke, E.M., Weilopolski, P.A., and Tkach, J.A. 1991. A comprehensive technical review of short T_R, fast magnetic resonance imaging techniques. *Rev. Magn. Reson. Med.* 3:53.

This article gives a modern review of the steady-state, fast imaging methods.

Haacke, E.M., Brown, R.W., Thompson, M.R., and Venkatesan, R. 1999. Magnetic Resonance Imaging: Physical Principles and Sequence Design. John Wiley & Sons, New York.

This text covers the technical aspects presented here, but in more detail, and also discusses more advanced materials.

Haase, A., Frahm, J., Matthei, D., Hannicke, W., and Merboldt, K.-D. 1986. FLASH imaging: Rapid imaging using low flip angle pulses. *J. Magn. Reson.* 67:256.

This article proposed different short T_E, fast imaging methods.

Hennig, J. 1991. Echoes—how to generate, recognize, use or avoid them in MR imaging sequences. Part I: Fundamental and not so fundamental properties of spin echoes. *Concepts Magn. Reson.* 3:125.

This text gives a modern review of the steady-state, fast imaging methods.

Hennig, J. 1991. Part II: Echoes in imaging sequences. *Concepts Magn. Reson.* 3:179.

This paper gives a modern review of the steady-state, fast imaging methods.

Oppelt, A., Graumann, R., Barfuss, H., Fischer, H., Hertl, W., and Schajor, W. 1986. FISP: A new fast MRI sequence. *Electromedica* 3:15.

This paper proposed different short T_E, fast imaging methods.

van der Muelen, P., Croen, J.P., and Cuppen, J.J.M. 1985. Very fast MR imaging by field echoes and small angle excitation. *Magn. Reson. Imaging* 3:297.

This article proposed different short T_E, fast imaging methods.

Contributed by Yu-Chung Norman Cheng and E. Mark Haacke
Case Western Reserve University
Cleveland, Ohio
and The MRI Institute for Biomedical Research
St. Louis, Missouri